# Nanodelivery Vehicles Induce Remote Biochemical Changes in vivo

Kristen N. Sikora, Laura J. Castellanos-García, Joseph M. Hardie, Yuanchang Liu, Michelle E. Farkas, Vincent M. Rotello, Richard W. Vachet\*

Department of Chemistry, University of Massachusetts Amherst, 240 Thatcher Way, Life Sciences Laboratory, Amherst, MA 01003

# **Corresponding Author**

\*E-mail: rwvachet@chem.umass.edu

Keywords: Nanodelivery, mass spectrometry imaging, nanoparticles, gold, lipids

#### **Abstract**

Nanomaterial-based platforms are promising vehicles for the controlled delivery of therapeutics. For these systems to be both efficacious and safe, it is essential to understand where the carriers accumulate and to reveal the site-specific biochemical effects they produce in vivo. Here, a dual-mode mass spectrometry imaging (MSI) method is used to evaluate the distributions and biochemical effects of anti-TNF-α nanoparticle stabilized capsules (NPSCs) in mice. It is found that most of the anticipated biochemical changes occur in sub-organ regions that are separate from where the nanomaterials accumulate. In particular, TNF- $\alpha$ -specific lipid biomarker levels change in immune cell-rich regions of organs, while the NPSCs accumulate in spatially isolated filtration regions. Biochemical changes that are associated with the nanomaterials themselves are also observed, demonstrating the power of matrix-assisted laser desorption/ionization (MALDI) MSI to reveal markers indicating possible off-target effects of the delivery agent. This comprehensive assessment using MSI provides spatial context of nanomaterial distributions and efficacy that cannot be easily achieved with other imaging methods, demonstrating the power of MSI to evaluate both expected and unexpected outcomes associated with complex therapeutic delivery systems.

### Introduction

Nanomaterials can be used to generate vehicles for delivery of therapeutics to organisms through general diffusion, tissue-specific localization, and active targeting at the cellular level. <sup>2,3</sup> These therapeutics can be encapsulated into their nanodelivery systems in a variety of ways, <sup>4,5</sup> such as part of an inorganic nanoparticle complex or a lipid bilayer droplet. These synthetic strategies not only allow for the controlled circulation of therapeutics, but also create the potential for more efficacious therapies through dose reduction, controlled circulation, and targeted delivery. <sup>4,6,7</sup> Inorganic nanomaterials are attractive for use in drug delivery applications due to their high stability, unique physical and chemical properties, and the exquisite synthetic control available through their surface chemistry. <sup>4,8</sup> The tunability of these modular systems provides many opportunities to deliver various cargos, including siRNA, <sup>9–11</sup> hydrophobic drugs, <sup>12,13</sup> and proteins. <sup>14</sup>

One of the goals in developing nanodelivery vehicles is controlling particle distribution *in vivo*, to yield the greatest therapeutic efficacy.<sup>15</sup> Unfortunately, studies focused on anti-cancer nanodelivery vehicles, for instance, report extremely low success rates in reaching target tumor sites (median, 0.7%).<sup>16</sup> Instead, most nanodelivery vehicles traffic to and through the mononuclear phagocytic system (MPS), predominantly the liver, spleen, and kidneys,<sup>16–19</sup> which filter them out, often resulting in secretion. However, these MPS organs have many heterogeneously distributed cell types with different functions,<sup>20,21</sup> and studies rarely address the sub-organ localization of any associated biochemical changes that occur *in vivo* upon injection of these materials. A spatial assessment of the biochemical changes caused by the nanomaterials, relative to their biodistributions, is necessary to better evaluate the efficacy of these nanodelivery vehicles.

Due to the nature of the MPS, nanodelivery agents and their cargo can cause biochemical effects that are not confined to their accumulation sites. For example, macrophages, which identify nanomaterials as foreign bodies, interact with other immune cells to elicit responses in their target organs (e.g. spleen), but often the responses that are generated can be in separate sub-organ regions from where the original foreign body was phagocytosed.<sup>22</sup> It is therefore important to assess whether individual nanomaterials and their cargo can induce biochemical changes at sites distant from where they accumulate, suggesting potential alternate/indirect means of therapy. In addition to organ-targeted treatments, the identification of non-localized biochemical changes would likewise be important for assessing the efficacy of therapies.

We report here the application of mass spectrometry imaging (MSI) methods to site-specifically track the *in vivo* distributions of nanodelivery systems, quantitatively establishing their biochemical effects at locations distant from their accumulation sites. Specifically, we use laser ablation-inductively coupled plasma mass spectrometry (LA-ICP-MS) and matrix-assisted laser desorption/ionization MS (MALDI-MS) based imaging approaches to monitor the sub-organ biodistributions and biochemical effects of a gold nanoparticle-based delivery platform. Unlike other imaging techniques, LA-ICP-MSI<sup>23-26</sup> and MALDI-MSI<sup>27,28</sup> can provide information about the spatial distributions of the nanomaterials and hundreds of biologically-relevant analytes *in situ*, thereby revealing essential biological information that can include unexpected details about molecular distributions. Using the two imaging modes together ensures that biometals and the inorganic components of the nanomaterials as well as biologically-relevant molecules are optimally detected,<sup>27</sup> as no one set of LA-ICP-MSI or MALDI-MSI analysis conditions allows detection of all compounds of interest.

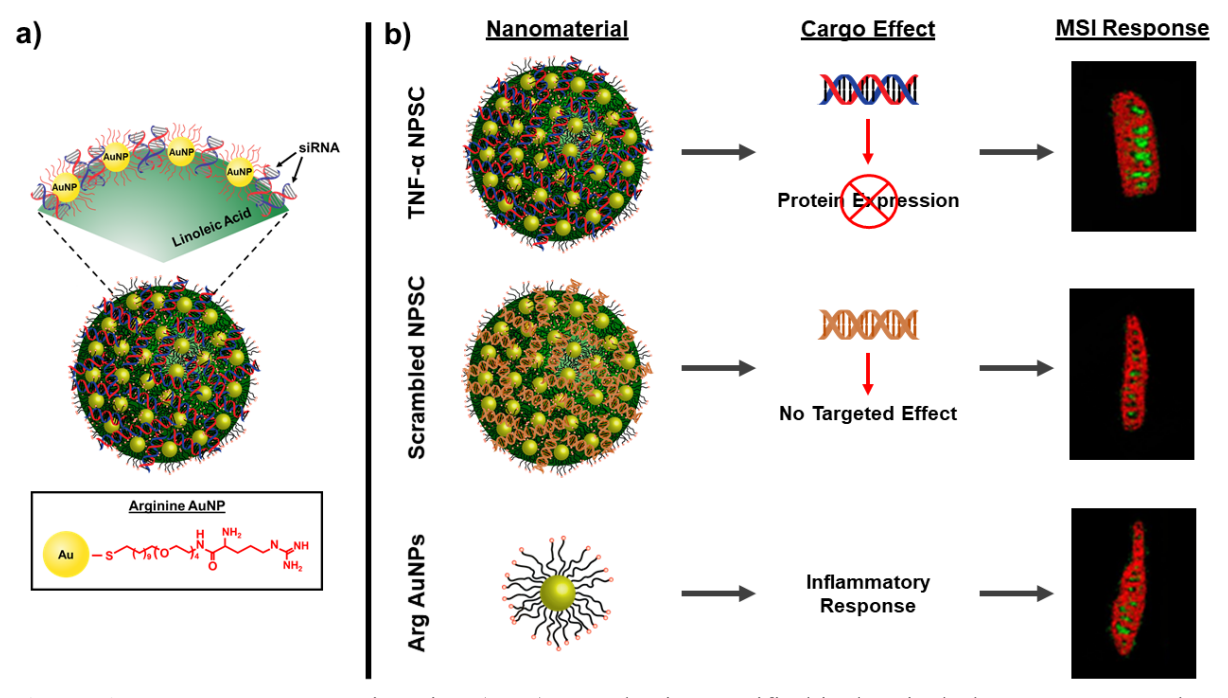


**Figure 1.** Mass spectrometry imaging (MSI) reveals site-specific biochemical changes *in vivo* when nanoparticle stabilized capsules (NPSCs) are injected into mice. a) NPSC design, including linoleic acid as an emulsifier, and arginine-capped AuNPs for forming a stable macrostructure via interactions with negatively charged siRNA cargo. b) NPSCs containing TNF-α-targeting siRNA (anti-TNF-α NPSCs), NPSCs containing scrambled, control siRNA (scrambled NPSCs), or arginine-based AuNPs (Arg AuNPs) were injected into mice and tissues (e.g. spleen and liver) were extracted and sectioned for LA-ICP-MS and MALDI-MS imaging. The anti-TNF-α NPSCs reduce the expression of the TNF-α protein by silencing the expression of TNF-α gene, whereas the scrambled NPSCs and the Arg AuNPs are expected to have no effect on this process. MS imaging (MSI) of tissues, with a spleen as an example in this figure, from mice injected with the nanomaterials indicate NP accumulation sites (red pixels) and site-specific changes in lipid biomarkers (green pixels).

As a testbed nanodelivery system in this work, we used gold nanoparticle-stabilized capsules (NPSCs) (Figure 1) that have demonstrated efficient delivery of proteins, siRNA, and small molecule drugs to the cytoplasm of cells. 9,12,29,30 TNF-α-targeting siRNA was utilized as the cargo in the current study, as NPSCs with this siRNA have been successfully used to knock-down this cytokine *in vitro* and in lipopolysaccharide (LPS)-stimulated mice by silencing the gene that expresses the TNF-α protein. 9 Although effective at decreasing TNF-α levels in LPS-stimulated mice, it is unknown whether TNF-α knockdown with the NPSCs causes the expected downstream signaling changes under normal conditions (i.e. no LPS stimulation). TNF-α suppression produces

predictable signaling changes in serum lipid levels,<sup>31</sup> which provides an opportune set of biomarkers to answer this question. Moreover, tracking these biomarkers in tissues via MALDI-MSI provides spatial context for these changes. When this spatial information is combined with the NPSC distributions that are revealed by LA-ICP-MSI, a more complete picture of how different cell types in MPS organs respond to these nanodelivery agents will be accessible.

Using MALDI- and LA-ICP-MS-based imaging methods synergistically, we find that nanodelivery agents can produce intended biochemical effects in locations separated from where the nanomaterials themselves accumulate. Moreover, the ability of MALDI-MS imaging to measure site-specific biochemical changes provides insight into how nanodelivery vehicles themselves influence inflammation pathways. In particular, we find that the presence of the gold nanoparticles (AuNPs) causes an inflammatory response in the tissues where they accumulate, as indicated by co-localized changes in glucosylceramide levels.

## **Results and Discussion**

NPSCs containing anti-TNF-α siRNA (anti-TNF-α NPSCs) were synthesized (see Methods) and injected into Balb/c mice. 9,27 After 48 h, the mice were sacrificed, and tissues were removed for analysis. As we have shown recently, TNF-α levels are effectively reduced in the serum of mice injected with these NPSCs,9 and ICP-MS measurements of acid-digested tissues of mice injected with the anti-TNF-α NPSCs reveal that the nanocarriers predominantly distribute to the liver and spleen (Figure S1).27 This *in vivo* distribution pattern is typical of positively charged nanomaterials. 16,23,32-34 Liver and spleen tissues were thus selected for MSI. Anti-TNF-alpha therapies mainly target macrophages and lymphocytes, both of which are in high concentration in these tissue types, 35 making the liver and spleen excellent tissues for the evaluation of these therapies. The distributions of lipid in tissues were determined by MALDI-MSI as a means of

monitoring downstream pathways known to be affected by TNF- $\alpha$  knockdown.<sup>31</sup> Distributions of gold in tissues were determined by LA-ICP-MSI as a means of tracking NPSC accumulation sites and/or the sites where any possibly degraded NPSCs accumulate. Unlike our recent work in which we first reported the ability of LA-ICP-MSI and MALDI-MSI to track nanomaterial and biomolecule distributions in the same tissue by simply overlaying the two images,<sup>27</sup> here we quantitatively combine (i.e. co-register) the two imaging modalities (see Methods). Co-registration of the images provides a more accurate correlation of the data from the two imaging modalities. We then apply these new approaches to different nanomaterial constructs to more fully understand how the components of the NPSCs affect spleen and liver tissue biochemistry.

Distribution and colocalization of nanocarrier and biochemical changes in the spleen

MALDI-MSI of spleen tissue sections was used to measure 52 different lipids, 44 of which responded to TNF-α in a predictable manner. Using the area under the curve (AUC) of receiver operating characteristic (ROC) curves, as are typically used in MALDI-MSI analyses, lipids were evaluated as successful binary classifiers between treated and control tissues (see Methods).<sup>27,38,39</sup> Based on the measured signals of the 44 lipids from at least three different tissue sections and three different mice, 33 lipids changed as predicted in the spleens of anti-TNF-α NPSC-injected mice when compared to control tissues (Table S1). The predicted changes are based on serum lipidomics experiments,<sup>31</sup> although the imaging data here provide new spatial information about these changes. Even though AuNPs have been used as matrices to facilitate lipid ionization in MALDI-MS,<sup>36,37</sup> control experiments indicate that the AuNP levels found in the tissues do not affect lipid ionization efficiencies (Figure S2).

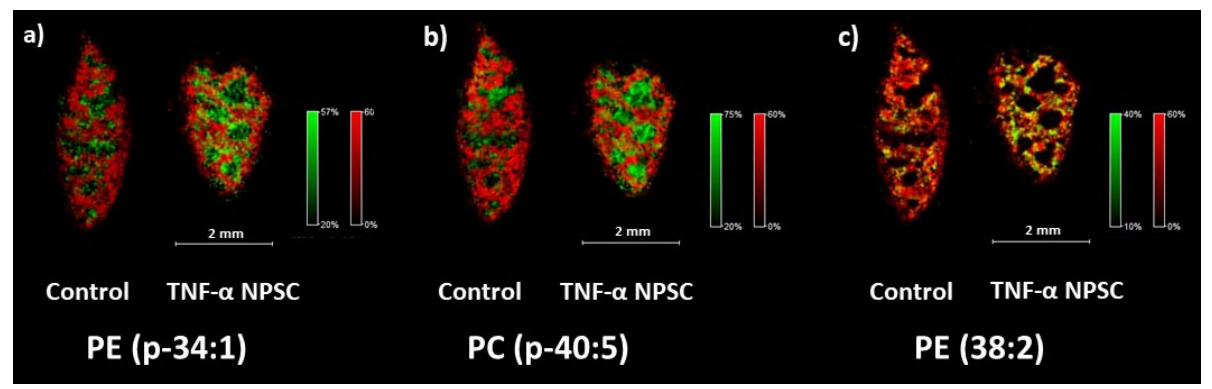
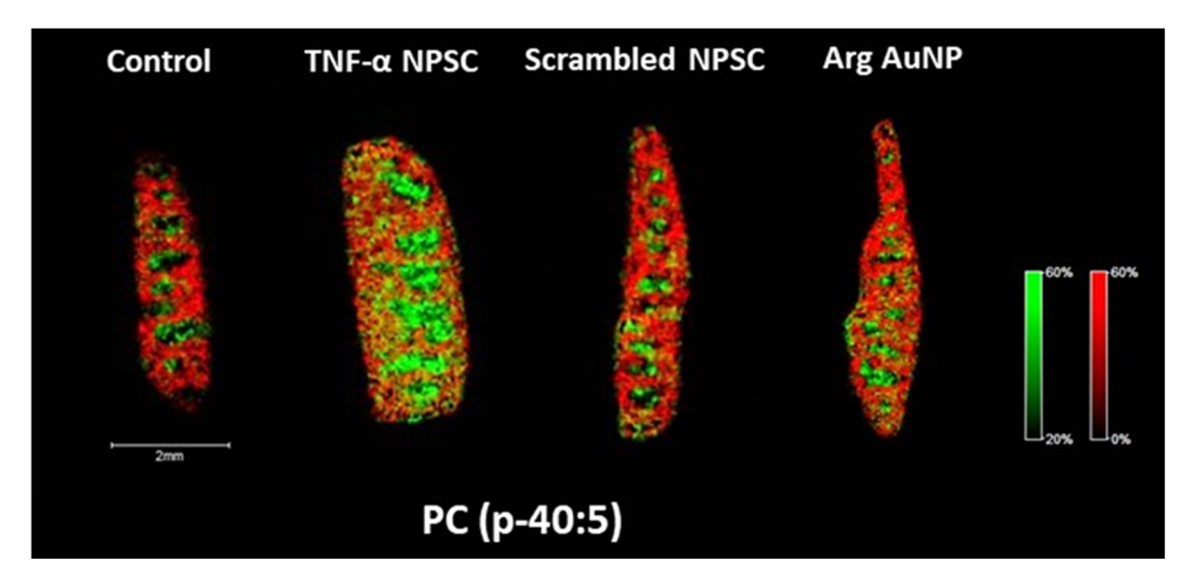


Figure 2. Representative MALDI-MS images of predicted lipid responses (green pixels) in anti-TNF- $\alpha$  NPSC-injected mouse spleen tissues (right within each image pair) compared to control spleen tissues (left within each image pair). Lipid ion intensity images are shown with heme B ion signals (red pixels) to show relative sub-organ distributions. Areas of high co-localization between a lipid and heme B are indicated by yellow pixels. Panels (a) and (b) are representative images of lipids that respond in the white pulp of anti-TNF- $\alpha$  NPSC spleen tissues. Panel (c) is a representative image of a lipid that responds in the red pulp.

By using the signal for heme B, which is a biomarker for the red pulp of the spleen,<sup>40</sup> the distributions of lipid changes were classified, using an image segmentation approach (see Methods), as occurring in the white pulp (no heme B signal) or red pulp (high heme B signal). For example, PE (p-34:1) and PC (p-40:5), which are plasmalogens known to be involved in anti-inflammatory and anti-oxidant responses in mammalian tissues,<sup>41</sup> increase in the lymphoid-rich white pulp (Figures 2a and b). Lipids signals that change in this lymphocyte-rich region of the spleen may be indicative of a downstream immunological response due to the NPSC cargo delivery. Conversely, PE (38:2), which is an unsaturated phosphatidylethanolamine involved in membrane curvature and fluidity during membrane fusion,<sup>42</sup> increases mostly in the red pulp (Figure 2c). Differentiating the sub-organ distributions of these specific biomarkers is important in determining if anti-inflammatory responses are occurring (i.e. in the splenic white pulp)<sup>43</sup> versus biochemical responses to cellular uptake (i.e. macrophages in the red pulp).<sup>23,43</sup> Overall, 79% of the 33 predicted lipid changes are found in the white pulp of the spleen tissue. These MSI data

indicate that the majority of the lipid responses are due to the efficacious delivery of the antiinflammatory siRNA therapeutic to the appropriate cell types.

Mice were also injected with scrambled (non-functional) siRNA-containing NPSCs (scrambled NPSCs) and arginine-functionalized NPs (Arg-AuNPs) that comprise the capsules to ensure that lipid changes observed in the treatment condition arise from biochemical changes induced by TNF-α knockdown, not the NPSC carrier itself (see Table S1 for Au levels in organs). Arg-AuNPs were chosen as a materials control because NPSCs without negatively-charged molecules like the siRNA are not stable. 12 Of the 44 lipids that are known to respond to TNFα knockdown, only 11 from scrambled NPSCs and five from Arg-AuNPs, have significantly altered levels in the spleens of mice (Table S1), indicating that the majority of the lipid changes observed in mice injected with anti-TNF-α NPSCs are due to target knockdown. In mice injected with the scrambled NPSCs, most lipids behave like PC (p-40:5) (Figure 3). The signal levels of these lipids do not change significantly compared to those of controls, regardless of whether they are found in the white pulp or red pulp. These data also further indicate that the AuNPs themselves are not influencing lipid detection, as even the presence of high concentrations of the Arg-AuNPs (10fold higher injected than NPSCs) do not lead to widespread changes in lipid signals compared to the untreated controls (Figure 3).



**Figure 3.** Representative MALDI-MS images of PC (p-40:5) response (green pixels) in anti-TNF- $\alpha$  and scrambled NPSC-injected mouse spleen tissues compared to control spleen tissues from an untreated mouse. Lipid ion intensity images are shown with heme B ion signals (red pixels) to show relative suborgan distributions. When compared to the control tissue from untreated mice, the anti-TNF- $\alpha$  NPSC exhibits an ROC AUC of 0.810, the scrambled NPSC an ROC AUC of 0.610, and the Arg-AuNPs an ROC AUC of 0.527.

LA-ICP-MSI was used to investigate the distribution of the anti-TNF-α NPSCs in the spleen (Figure 4). In these images, iron signals were used to discern the blood-rich red pulp from the white pulp (Figure 4d). Visual comparison of the gold (Figure 4b) and iron distributions indicate that the two metals have similar distributions, and this similarity is even more apparent from the overlaid images (Figure 4c). Based on a quantitative pixel analysis of the images in Figure 4c, a Pearson correlation analysis indicates a 67% correlation between the gold and iron distributions. LA-ICP-MS imaging analysis of three spleen tissue slices from three mice (i.e. total of nine images) lead to an average correlation of 65%. Overall, these results indicate that the gold carrier predominantly accumulates in the red pulp of the spleen. A very similar observation is made for spleen tissues from mice injected with scrambled NPSCs: NPSCs accumulate mostly in the red pulp of the spleen (e.g. Figure S3).

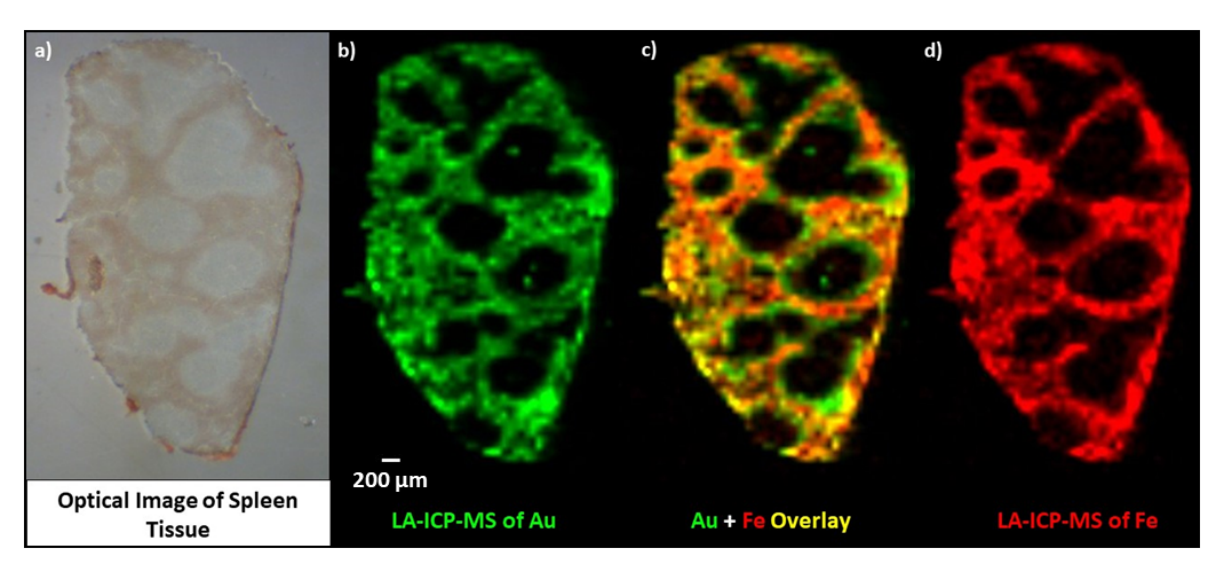


**Figure 4.** Representative optical and LA-ICP-MS images of anti-TNF-α NPSC-injected mouse spleen. (a) Optical camera image. (b) Reconstructed LA-ICP-MS image of gold at 50 μm resolution, single color scale. (c) Gold (green) and iron (red) LA-ICP-MS overlaid images. Yellow pixels indicate analyte overlap. (d) Reconstructed LA-ICP-MS image of iron at 50 μm resolution, single color scale.

While gold primarily accumulates in the red pulp, 79% of the predicted lipid changes due to TNF-α knockdown actually occur in the white pulp of the spleen (Figure 2a & 2b), indicating that the intended biochemical effect occurs in a different location from where the NPSCs accumulate. To confirm these results quantitatively, the LA-ICP-MS and MALDI-MS images were coregistered, 44,45 allowing correlations on a pixel-by-pixel basis to be calculated for gold and each lipid. Based on these correlation analyses, 25 of the 33 lipids that change as expected correlate negatively with the distribution of the NPSCs (Figure 5), whereas only eight of them correlate positively with the NPSCs. As a whole, these results mean that most of the TNF-α knockdown-related changes occur spatially removed from the site of the nanodelivery vehicle accumulation.

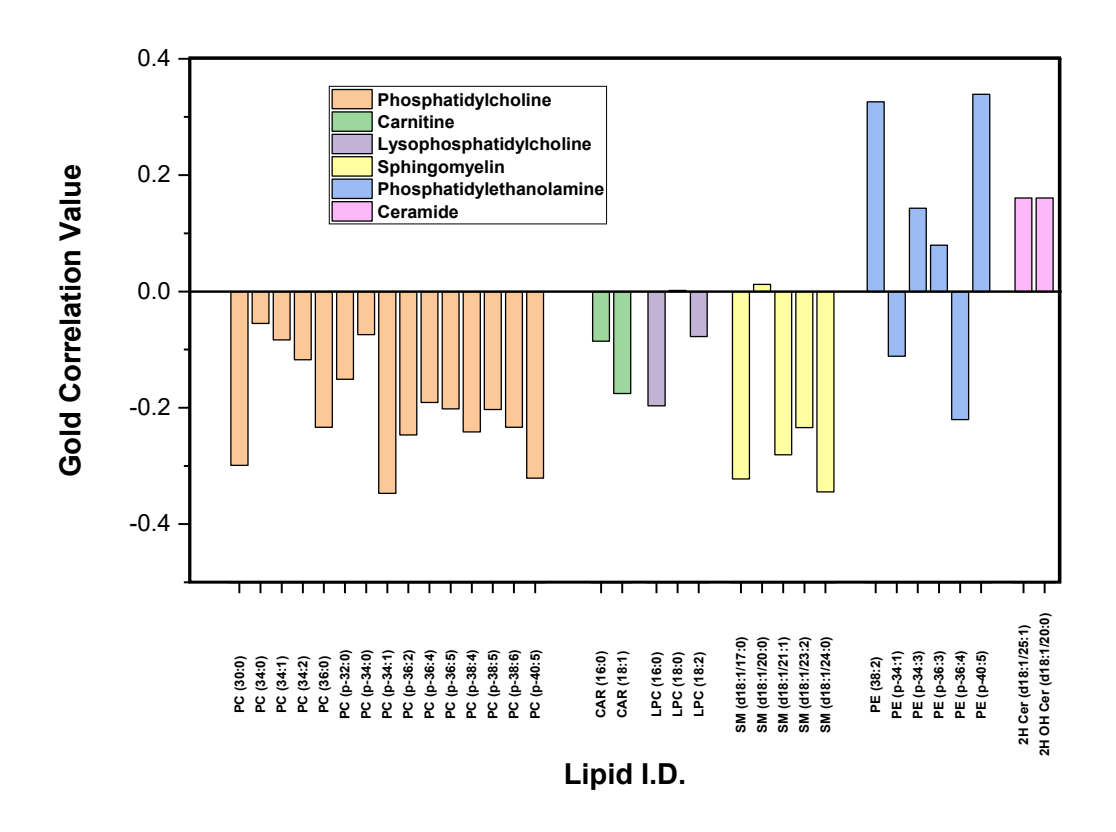


**Figure 5.** Correlation plot of MALDI-MSI lipid distributions and LA-ICP-MS gold distributions in splenic tissue of anti-TNF-α NPSC-treated mice. Lipids are separated by class from left to right: phosphatidylcholines, carnitines, lysophosphatidylcholines, sphingomyelins, phosphatidylethanolamines, and ceramides. Lipids with values close to +1 have a strong positive *Distribution and colocalization of nanocarrier and biochemical changes in the liver* 

NPSC and lipid distributions were also assessed in the liver due to the high gold content in this tissue (Figure S1). In the liver, 40 TNF-α-specific lipids were measured by MALDI-MS, and 18 of these 40 lipids undergo the predicted changes when the anti-TNFα NPSCs are injected (Table S2). Fewer lipids are confidently measured in the liver as compared to the spleen because the overall MALDI-MS ion signals in the liver tissues were lower on average. Moreover, we only considered data for the lipids that could be detected in all the liver tissue sections from all three nanomaterial types for all three mice. In tissue sections from the mice injected with scrambled NPSCs and Arg-AuNPs, only nine and five, respectively, of the 40 lipids undergo significant changes, indicating that the lipid changes were again primarily due to TNF-α knockdown. Unlike

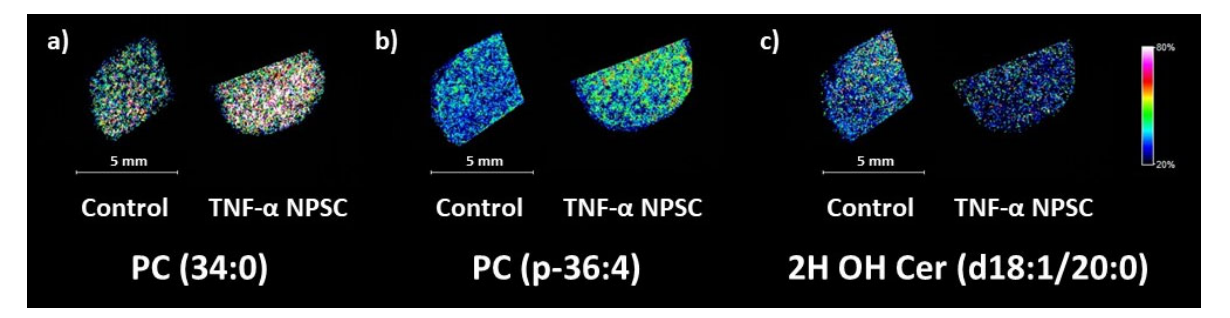


**Figure 6.** Representative MALDI-MS images of predicted lipid responses in anti-TNF- $\alpha$  NPSC-injected mouse liver tissues (right within each image pair) compared to control liver tissues from untreated mice (left within each image pair). Panels (a) and (b) are representative images of lipids that increase in anti-TNF- $\alpha$  NPSC-treated liver tissues. Panel (c) is a representative image of a lipid that decreases in anti-TNF- $\alpha$  NPSC-treated liver tissues.

in the spleen, which has readily distinguishable sub-organ regions that allow lipid distributions to be visually classified, the liver sections have smaller, more heterogeneous features that usually make it difficult to visually classify lipid distributions into different sub-organ regions (Figure 6). Moreover, depending on how the liver is sectioned, large areas of connective tissue can be seen (e.g. white outline area in Figure 7a), sometimes leading to differences in the apparent morphology of the tissue sections. Despite these occasional differences from tissue section to tissue section, the LA-ICP-MS images of the liver reveal that gold has a punctate distribution in the liver (e.g. Figure 7b). Previous work has shown that positively-charged AuNPs accumulate in liver hepatocytes, giving rise to such a distribution,<sup>23</sup> suggesting that the positively-charged NPs used in the NPSCs studied here likely also accumulate in hepatocytes. Images from liver tissues of mice injected with scrambled NPSCs show the same punctate gold distribution as observed in the treatment condition (Figure S4).

When we compare the distributions of gold and the lipids that change upon TNF- $\alpha$  knockdown after co-registering the LA-ICP-MS and MALDI-MS images, we again find that the lipid changes generally do not correlate with gold accumulation sites (Figure 8). The majority (13 of 18) of the predicted TNF- $\alpha$  induced changes occur throughout the liver tissue, and do not correlate strongly

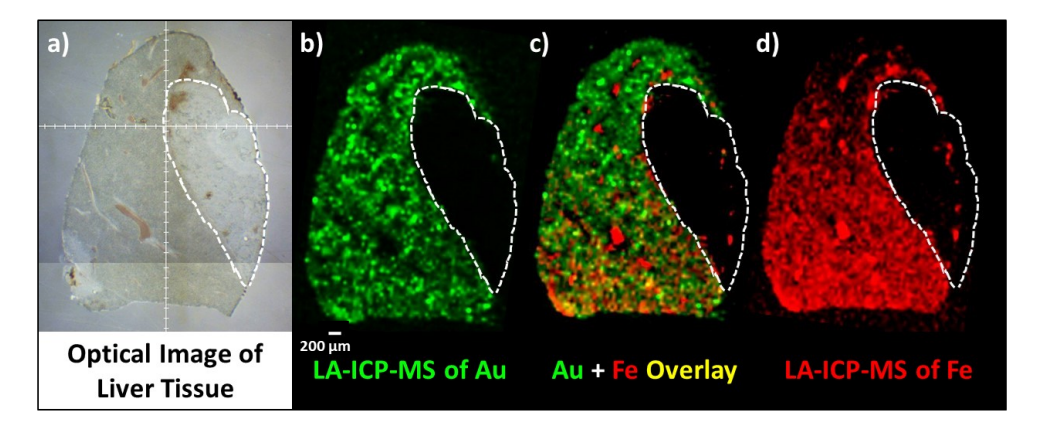


**Figure 7**. Optical and LA-ICP-MS images of liver tissue from an anti-TNF-α NPSC-treated mouse, showing a pronounced region of connective tissue (outlined by dotted white line). (a) Optical camera image. (b) Reconstructed LA-ICP-MS image of gold at 50 μm resolution, single color scale. (c) Gold (green) and iron (red) LA-ICP-MS overlay images. (d) Reconstructed LA-ICP-MS image of iron at 50 μm resolution, single color scale. Gold and iron are not readily observed in the connective tissue of mice, as indicated by the white outline in each image.

with the gold carrier distribution. These data suggest that the lipid responses also occur mostly independent of nanodelivery vehicle distributions in the liver, as was observed in the spleen.

Even though sub-organ regions of the liver are not visually apparent, some lipids are known to associate with certain regions of the liver, <sup>46</sup> as illustrated in Figure 9, allowing the distribution of gold to be assigned to individual sub-organ regions. By co-registering LA-ICP-MS images that report on the carrier distribution (e.g. Figure 7) with MALDI-MS images that indicate lipid distributions in different sub-organ regions (e.g. Figure 9), NPSCs are found to accumulate mostly in the parenchyma (78%), which is the functional portion of the liver tissue containing hepatocytes. The remaining nanomaterial is found in the veins (22%), with no significant amounts found in the bile ducts or connective tissue. These results are consistent with previous work that showed accumulation of positively-charged AuNPs in the liver hepatocytes. <sup>23</sup> Of the TNF-α-related lipid changes in the liver, 34% occur in the connective tissue, 32% in the parenchyma, 18% in the veins, and 16% in the bile ducts. Interestingly, the connective tissue is known be the main source of liver mast cells, <sup>47</sup> which are heavily involved in transmitting signals during an inflammatory response

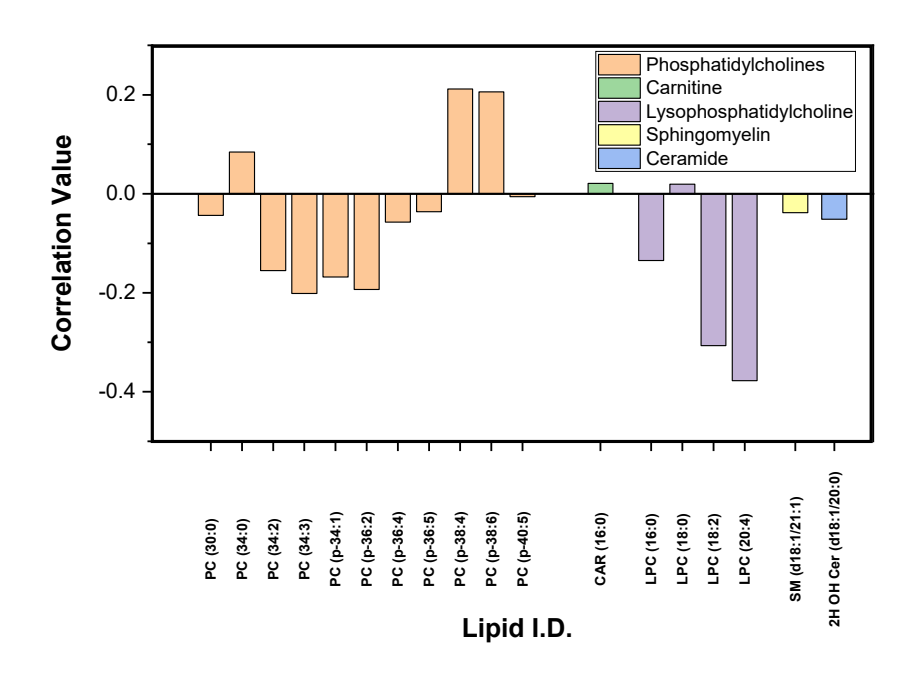


**Figure 8.** Correlation plot of MALDI-MSI lipid distributions and LA-ICP-MS gold distributions in liver tissue of anti-TNF-α NPSC-treated mice. Lipids are separated by class from left to right: phosphatidylcholines, carnitines, lysophosphatidylcholines, sphingomyelins, phosphatidylethanolamines, ceramides. Lipids with values close to +1 have a strong positive correlation with gold distribution; lipids with values close to -1 have a strong negative correlation with gold distribution; lipids with values close to zero have no significant correlation with gold.

in the liver. 48 Overall, a cumulative 68% (34% + 18% + 16%) of the lipid changes in the liver occur in regions with no significant gold accumulation, indicating that the effects of the anti-TNF- $\alpha$  therapy primarily occur in regions remote from where the NPSC carriers accumulate.

## Distribution of unexpected lipid changes in tissues of NPSC-injected mice

The dual-mode imaging method that is utilized here reveals not only that NPSCs elicit biochemical changes in the spleen and liver at locations remote from where they accumulate, but also that some biochemical changes are likely caused by the nanocarrier itself. The inherently multiplexed nature of MALDI-MS imaging along with the gold distributions obtained from LA-ICP-MS allow us to discern unexpected effects of the carrier. The MALDI-MSI data are a complex set of molecular information, and a full accounting of the unexpected effects of the carrier are

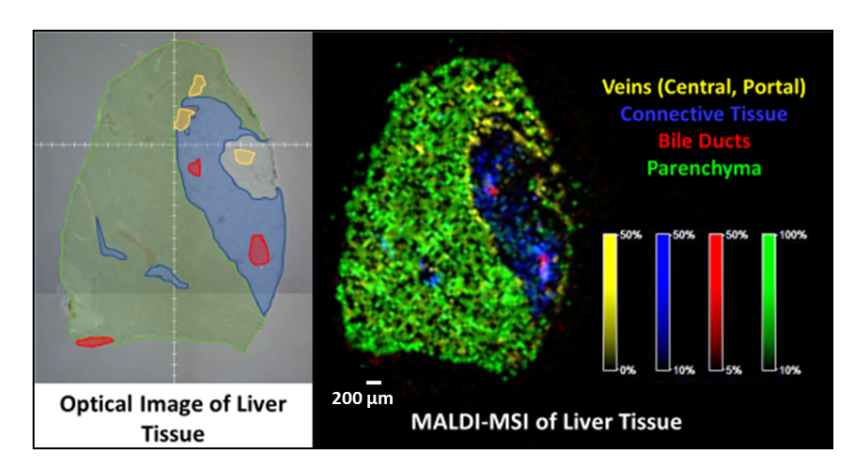


**Figure 9**. Representative optical and MALDI-MSI liver images that are utilized to classify sub-organ regions of liver tissue. Veins are indicated by yellow pixels, connective tissue by blue pixels, bile ducts by red pixels, and parenchyma by green pixels.

beyond the scope of this work. However, as an example of the information that MSI can provide, one notable lipid that changes unexpectedly in mice injected with all nanomaterial constructs (i.e. anti-TNF-α NPSCs, scrambled NPSCs, and Arg-AuNPs) is glucosylceramide. The signal for this lipid increases in both spleen and liver tissues and is found to positively correlate with gold distributions from tissues injected with each of the nanomaterials (Figures S5 and S6). After a coregistration analysis of the LA-ICP-MS and MALDI-MS images of the liver tissues, glucosylceramide is found to have a 77% correlation with gold in the anti-TNF-α NPSC-containing tissues, 93% in the scrambled siRNA NPSC-containing tissues, and 90% in the Arg-AuNP containing tissues (Figure S6). Ceramide is a pro-apoptotic mediator that glucosylceramide synthase (GCS) converts to the inert compound glucosylceramide.<sup>49</sup> Glucosylceramides are biomarkers involved in inflammation and are specifically associated with macrophage uptake in the liver, spleen, and kidneys.<sup>50</sup> Observation of this lipid increase in both the liver and spleen following treatment with all three nanomaterial constructs suggests that the AuNPs themselves are eliciting an inflammatory response. Future work will be necessary to fully understand the nature of this effect. This assessment using dual-mode imaging and registration provides a direct and quantitative evaluation of the effects of the nanomaterials themselves and is a powerful way to evaluate both the efficacy and side effects of nanomaterials *in vivo*.

#### **Conclusions**

MS imaging techniques were employed to monitor the distribution and co-localization of a nanodelivery system and its biochemical effects in various tissue types. Using MALDI and LA-ICP MS techniques, we demonstrate that the majority of the expected downstream biochemical changes occur in regions distant from where the nanodelivery system accumulates. Specifically, while changes in siRNA or protein levels are not measured directly by MSI, we find that anti-TNFα NPSCs cause expected changes in lipid biomarkers, primarily in the white pulp of the spleen, whereas the NPSCs themselves accumulate in the red pulp. Similarly, anti-TNF-α NPSCs elicit expected changes in liver lipid biomarkers mostly in veins, connective tissue, and bile ducts, while the NPSCs accumulate in the parenchyma, where fewer biomarker changes occur. These observations demonstrate that nanodelivery vehicles can generate the desired biochemical responses even though they may accumulate in different locations. This behavior of nanodelivery agents might suggest an indirect means of therapy, which could be particularly important for anticancer nanodelivery agents that accumulate inefficiently in tumors. Another important result from the work described here is that information-rich MALDI-MS imaging is capable of identifying unanticipated changes in tissue biochemistry caused by the presence of nanodelivery vehicles. In this way, MALDI-MSI generates new molecular-level information that when complemented by traditional biochemical assays could lead to new insight into potential off-target effects that may be caused by nanodelivery systems. Future work will investigate potential off-target effects more extensively.

#### Methods

Synthesis of nanoparticles and nanoparticle stabilized capsules

Arg-AuNPs and NPSCs were synthesized according to a previous report. Pietfly, 1-pentaethiol protected AuNPs (Au-C5) were synthesized via the Brust-Sciffrin two-phase synthesis. Arg-AuNPs were then synthesized by the Murray place-exchange method. NPSCs were generated by emulsifying 1 μL linoleic acid with 1 μM Arg-AuNPs in PBS. A 2.5 μM aliquot mixture was then combined with 1 μM siRNA. The mixture was then incubated at room temperature before injection. Physical characterization of the anti-TNF-α NPSCs, scrambled NPSCs, and Arg-AuNPs was performed via dynamic light scattering (Table S3). Characterization of the NPSCs and Arg-AuNPs followed procedures that have been previously reported. Pietgle S3 as the exact same materials that were used in that study were used in the current study.

### Animal experiments and tissue preparation

All animal protocols were approved by the University of Massachusetts Amherst Institutional Animal Care and Use Committee (IACUC), guided by the U.S. Animal Welfare Act and U.S. Public Health Service Policy. Balb/c mice (female, 8-week-old) were obtained from Charles River Laboratories, Inc. (Wilmington, MA). Mice were held in controlled climates ( $22 \pm 2$  °C temperature, 12 h light/dark daily cycle) with free access to food and water. Mice were randomly selected for control and nanomaterial treatment. Three mice were selected for each treatment batch including, control, anti-TNF- $\alpha$  NPSCs, scrambled NPSCs, and Arg-AuNPs, totaling 12 mice. Each mouse was tail-vein-injected with 200  $\mu$ L of either PBS (control), 2.5  $\mu$ M of NPSCs, or 2.5  $\mu$ M of Arg-AuNPs. Following 48 h of nanomaterial circulation, mice were sacrificed via carbon

dioxide inhalation and cervical dislocation. Mouse tissues were promptly removed, flash frozen in liquid nitrogen, and stored at -80 °C until sectioning for MS imaging. A portion of each retrieved tissue was removed for acid digestion and ICP-MS analysis to assess total gold concentrations (Figure S1). Flash-frozen tissues were sectioned into 12 µm slices via a LEICA CMM1850 cryostat, thaw-mounted onto ITO slides (MALDI-MS) or glass slides (LA-ICP-MS), and desiccated under vacuum for 1 h. Bruker ImagePrep apparatus was used to spray a 25 mg/mL 2,5-DHB solution (1:1 methanol:water) onto the tissues intended for MALDI imaging analysis.

## Dual-Mode Imaging Analysis

MALDI-MSI was conducted using a Bruker ultrafleXtreme MALDI-TOF/TOF instrument at 50 µm resolution unless otherwise indicated. All experiments were performed with at least three different tissue sections from each of the three injected mouse replicates, for a total of nine MALDI-MS images per sample treatment. All treated tissues (NPSC or Arg-AuNP-injected) were run simultaneously with control tissue samples to ensure reproducibility. MS/MS experiments were performed via LIFT cell with collision-induced dissociation to confirm biomolecule identities.

LA-ICP-MS imaging was conducted using PerkinElmer NEXION 300 ICP-MS coupled with a Teledyne CETAC LSX-213 G2 laser ablation system which was attached to the ICP-MS via Teflon tubing. Tissues were ablated at a spot size of either 50 or 25 μm with a 15 μm/s scan rate, 10 Hz laser frequency, 0.6 L/min He carrier gas flow, and 10 s shutter delay. Images were reconstructed according to previous reports.<sup>23,25,27,32</sup> LA-ICP-MS images were acquired on three tissue sections from each of the three treated mice.

#### Statistical evaluation

MALDI-MSI images were normalized and processed in SCiLS Lab 2015b (Bruker), as previously reported.<sup>27</sup> In brief, baseline subtraction was conducted using the TopHat, followed by total ion count (TIC) normalization, peak picking, and discriminative value determination using both receiver operating characteristic (ROC) curves and ion abundance box-and-whisker plots. ROC curves are statistical tests used to determine how well a variable (e.g. distribution of lipid ion signals) preforms as a binary classifier between two systems. For the MALDI-MSI analyses, a nanomaterial-treated mouse tissue and a control mouse tissue were the two systems that were compared. ROC curves are generated by assessing the threshold response of the ion signal abundance distributions of a given measured molecule in the two tissues. The analysis considers plots of the true positive rates (or total pixels from tissue 1 above the threshold value, divided by total pixels of tissue 1) versus the false positive rates (or total pixels from tissue 2 above the threshold value, divided by total pixels of tissue 2). The area under these ROC curves can then be used as a gauge for how well the m/z value distinguishes between the two tissue types. ROC area under the curve (AUC) thresholds of greater than 0.65 for analyte increases or lower than 0.35 for analyte decreases were used to distinguish significant differences between tissues. 27,38,39

## Image Segmentation

Segmentation of MALDI-MSI tissue images was performed using a k-means clustering algorithm in SCiLS Lab 2015b. All images were preprocessed with normalization and peak selection before applying the segmentation algorithm. Using this algorithm, the similarities of the spectra are statistically evaluated, and those spectra that are determined to be similar are grouped into single clusters. Each separate cluster can then be used to represent sub-organ regions in a

given tissue section. This image segmentation approach was used to automatically classify red pulp and white pulp regions in MALDI-MS images of spleen tissue sections. Confirmation of these classifications was done by manually spot-checking the relative ion intensities of the heme signals in the pixels that clustered as red pulp regions (high heme ion signal) as compared to those that clustered as white pulp regions (no heme ion signal).

## Correlation plot calculations

Correlation plot calculations for quantitatively comparing the LA-ICP-MS and MALDI-MS imaging data were made in Python using Pearson's correlation analysis. Briefly, MALDI-MS and LA-ICP-MS data were transformed into the same X-Y scale using an analogous approach to previous work. Hands were co-registered using a non-linear registration algorithm in Python. The SimpleElastix library in Python was applied with the MALDI data set as the fixed image and the LA-ICP-MS data set as the moving image. Once tissues were properly co-registered on a pixel-by-pixel basis, a Pearson's correlation analysis was conducted in Python using the SciPy library. Each analyte was quantitatively compared against each other to assess the strength of association between the two variables with -1 being an absolute negative correlation, +1 being an absolute positive correlation, and 0 being no correlation.

#### **Conflicts of interest**

There are no conflicts to declare.

### Acknowledgements

This research was supported by the NSF (CHE-1808199) and the NIH (EB022641).

## **Supporting Information Available**

Lipid response tables, ICP-MS tissue digestions, and control LA-ICP-MS images can be found in the supporting information.

#### References

- (1) T. Borel and C. M. Sabliov, Nanodelivery of Bioactive Components for Food Applications: Types of Delivery Systems, Properties, and Their Effect on ADME Profiles and Toxicity of Nanoparticles. *Annu. Rev. Food Sci. Technol.* 2014, **5**, 197–213.
- (2) J. K. Patra, G. Das, L. F. Fraceto, E. V. R. Campos, M. del P. Rodriguez-Torres, L. S. Acosta-Torres, L. A. Diaz-Torres, R. Grillo, M. K. Swamy, S. Sharma, S. Habtemariam and H.-S. Shin, Nano Based Drug Delivery Systems: Recent Developments and Future Prospects. *J. Nanobiotechnol.* 2018, **16**, 71.
- (3) J. H. Adair, M. P. Parette, E. I. Altinoğlu and M. Kester, Nanoparticulate Alternatives for Drug Delivery. *ACS Nano* 2010, **4**, 4967-4970.
- (4) T. C. Yih and M. Al-Fandi, Engineered Nanoparticles as Precise Drug Delivery Systems. *J. Cell. Biochem.* 2006, **97**, 1184-1190.
- (5) X. Yu, I. Trase, M. Ren, K. Duval, X. Guo, and Z. Chen, Design of Nanoparticle-Based Carriers for Targeted Drug Delivery. *J. Nanomater.* 2016, 1087250.
- (6) M. De, P. S. Ghosh and V. M. Rotello, Applications of Nanoparticles in Biology. *Adv. Mater.* 2008, **20**, 4225–4241.
- (7) B. Kumar, K. Jalodia, P. Kumar, and H. K. Gautam, Recent Advances in Nanoparticle-Mediated Drug Delivery. *J. Drug Deliv. Sci. Technol.* 2017, **41**, 260–268.
- (8) E. C. Dreaden, A. M. Alkilany, X. Huang, C. J. Murphy and M. A. El-Sayed, The Golden Age: Gold Nanoparticles for Biomedicine. *Chem. Soc. Rev.* 2012, **41**, 2740.
- (9) Y. Jiang, J. Hardie, Y. Liu, M. Ray, X. Luo, R. Das, R. F. Landis, M. E. Farkas, and V. M. Rotello, Nanocapsule-Mediated Cytosolic SiRNA Delivery for Anti-Inflammatory Treatment. *J. Control. Release* 2018, **283**, 235–240.
- (10) M. T. Abrams, M. L. Koser, J. Seitzer, S. C. Williams, M. A. Dipietro, W. Wang, A. W. Shaw, X. Mao, V. Jadhav, J. P. Davide, P. A. Burke, A. B. Sachs, S. M. Stirdivant and L. Sepp-Lorenzino, Evaluation of Efficacy, Biodistribution, and Inflammation for a Potent SiRNA Nanoparticle: Effect of Dexamethasone Co-Treatment. *Mol. Ther.* 2010, 18, 171–180.
- (11) K. A. Whitehead, R. Langer and D. G. Anderson, Knocking down Barriers: Advances in

- SiRNA Delivery. Nat. Rev. Drug Discov. 2009, 8, 129–138.
- (12) X. C. Yang, B. Samanta, S. S. Agasti, Y. Jeong, Z. J. Zhu, S. Rana, O. R. Miranda and V. M. Rotello, Drug Delivery Using Nanoparticle-Stabilized Nanocapsules. *Angew. Chem. Int. Ed.* 2011, 50, 477–481.
- (13) D. Hofmann, C. Messerschmidt, M. B. Bannwarth, K. Landfester and V. Mailänder, Drug Delivery without Nanoparticle Uptake: Delivery by a Kiss-and-Run Mechanism on the Cell Membrane. *Chem. Commun.* 2014, **50**, 1369–1371.
- (14) R. Tang, C. S. Kim, D. J. Solfiell, S. Rana, R. Mout, E. M. Velázquez-Delgado, A. Chompoosor, Y. Jeong, B. Yan, Z.-J. Zhu, C. Kim, J. A. Hardy and V. M. Rotello, Direct Delivery of Functional Proteins and Enzymes to the Cytosol Using Nanoparticle-Stabilized Nanocapsules. *ACS Nano* 2013, 7, 6667–6673.
- (15) W. H. De Jong, W. I. Hagens, P. Krystek, M. C. Burger, A. J. A. M. Sips and R. E. Geertsma, Particle Size-Dependent Organ Distribution of Gold Nanoparticles after Intravenous Administration. *Biomaterials* 2008, **29**, 1912–1919.
- (16) S. Wilhelm, A. J. Tavares, Q. Dai, S. Ohta, J. Audet, H. F. Dvorak and W. C. W. Chan, Analysis of Nanoparticle Delivery to Tumours. *Nat. Rev. Mater.* 2016, **1**, 16014.
- (17) C. Gunawan, M. Lim, C. P. Marquis and R. Amal, Nanoparticle-Protein Corona Complexes Govern the Biological Fates and Functions of Nanoparticles. *J. Mater. Chem. B* 2014, **2**, 2060–2083.
- (18) Y. Zhang, K. Cai, C. Li, Q. Guo, Q. Chen, X. He, L. Liu, Y. Zhang, Y. Lu, X. Chen, T. Sun, Y. Huang, J. Cheng and C. Jiang, Macrophage-Membrane-Coated Nanoparticles for Tumor-Targeted Chemotherapy. *Nano Lett.* 2018, **18**, 1908–1915.
- (19) A. Albanese, P. S. Tang and W. C. W. Chan, The Effect of Nanoparticle Size, Shape, and Surface Chemistry on Biological Systems. *Annu. Rev. Biomed. Eng.* 2012, **14**, 1–16.
- (20) K. B. Halpern, R. Shenhav, O. Matcovich-Natan, B. Toth, D. Lemze, M. Golan, E. E. Massasa, S. Baydatch, S. Landen, A. E. Moor, A. Brandis, A. Giladi, A. S. Avihail, E. David, I. Amit and S. Itzkovitz. Single-cell spatial reconstruction reveals global division of labour in the mammalian liver. *Nature* 2017, **542**, 352-356.
- (21) B. J. Stewart, J. R. Ferdinand, M. D. Young, T. J. Mitchell, K. W. Loudon, A. M. Riding, N. Richoz, G. L. Frazer, J. U. L. Staniforth, F. A. V. Braga, R. A. Botting, D.-M. Popescu, R. Vento-Tormo, E. Stephenson, A. Cagan, S. J. Farndon, K. Polanski, M. Efremova, K. Green, M. Del Castillo Velasco-Herrera, C. Guzzo, G. Collord, L. Mamanova, T. Aho, J. N. Armitage, A. C. P. Riddick, I. Mushtaq, S. Farrell, D. Rampling, J. Nicholson, A. Filby, J. Burge, S. Lisgo, S. Lindsay, M. Bajenoff, A. Y. Warren, G. D. Stewart, N. Sebire, N. Coleman, M. Haniffa, S. A. Teichmann, S. Behjati and M. R. Clatworthy. Spatiotemporal immune zonation of the human kidney. *Science* 2019, 365, 1461–1466.
- (22) H. Borges Da Silva, R. Fonseca, R. M. Pereira, A. A. Cassado, J. M. Álvarez and M. R. D'Império Lima, Splenic Macrophage Subsets and Their Function during Blood-Borne Infections. *Front. Immunol.* 2015, **6**, 480.

- (23) S. G. Elci, Y. Jiang, B. Yan, S.T. Kim, K Saha, D. F. Moyano, G. Yesilbag Tonga, L. C. Jackson, V. M. Rotello and R. W. Vachet, Surface Charge Controls the Suborgan Biodistributions of Gold Nanoparticles. *ACS Nano* 2016, **10**, 5536–5542.
- (24) S. G. Elci, G. Yesilbag Tonga, B. Yan, S. T. Kim, C. S. Kim, Y. Jiang, K. Saha, D. F. Moyano, A. L. M. Marsico, V. M. Rotello and R. W. Vachet, Dual-Mode Mass Spectrometric Imaging for Determination of *in vivo* Stability of Nanoparticle Monolayers. *ACS Nano* 2017, **11**, 7424–7430.
- (25) L. J. Castellanos-García, S. G. Elci and R. W. Vachet, Reconstruction, Analysis, and Segmentation of LA-ICP-MS Imaging Data Using Python for the Identification of Sub-Organ Regions in Tissues. *Analyst* 2020, **145**, 3705-3712.
- (26) A. Sussulini, J. S. Becker and J. S. Becker, Laser Ablation ICP-MS: Application in Biomedical Research. *Mass Spectrom. Rev.* 2017, **36**, 47-57.
- (27) K. N. Sikora, J. M. Hardie, L. J. Castellanos-García, Y. Liu, B. M. Reinhardt, M. E. Farkas, V. M. Rotello and R. W. Vachet, Dual Mass Spectrometric Tissue Imaging of Nanocarrier Distributions and Their Biochemical Effects. *Anal. Chem.* 2020, **92**, 2011–2018.
- (28) A. R. Buchberger, K. DeLaney, J. Johnson and L. Li, Mass Spectrometry Imaging: A Review of Emerging Advancements and Future Insights. *Anal. Chem.* 2018, **90**, 240-265.
- (29) J. Hardie, Y. Jiang, E. R. Tetrault, P. C. Ghazi, G. Y. Tonga, M. E. Farkas and V. M. Rotello, Simultaneous Cytosolic Delivery of a Chemotherapeutic and siRNA Using Nanoparticle-Stabilized Nanocapsules. *Nanotechnology* 2016, **27**, 374001.
- (30) Y. Jiang, R. Tang, B. Duncan, Z. Jiang, B. Yan, R. Mout and V. M. Rotello, Direct Cytosolic Delivery of SiRNA Using Nanoparticle-Stabilized Nanocapsules. *Angew. Chem. Int. Ed.* 2015, **54**, 506–510.
- (31) M. Wallace, C. Morris, C. M. O'Grada, M. Ryan, E. T. Dillon, E. Coleman, E. R. Gibney, M. J. Gibney, H. M. Roche and L. Brennan, Relationship between the Lipidome, Inflammatory Markers and Insulin Resistance. *Mol. Biosyst.* 2014, 10, 1586–1595.
- (32) S. G. Elci, B. Yan, S. T. Kim, K. Saha, Y. Jiang, G. A. Klemmer, D. F. Moyano, G. Y. Tonga, V. M. Rotello and R. W. Vachet, Quantitative Imaging of 2 nm Monolayer-Protected Gold Nanoparticle Distributions in Tissues Using Laser Ablation Inductively-Coupled Plasma Mass Spectrometry (LA-ICP-MS). *Analyst* 2016, **141**, 2418–2425.
- (33) B. Yan, S. T. Kim, C. S. Kim, K. Saha, D. F. Moyano, Y. Xing, Y. Jiang, A. L. Roberts, F. S. Alfonso, V. M. Rotello and R. W. Vachet, Multiplexed Imaging of Nanoparticles in Tissues Using Laser Desorption/Ionization Mass Spectrometry. *J. Am. Chem. Soc.* 2013, 135, 12564–12567.
- (34) R. R. Arvizo, O. R. Miranda, D. F. Moyano, C. A. Walden, K. Giri, R. Bhattacharya, J. D. Robertson, V. M. Rotello, J. M. Reid and P. Mukherjee, Modulating Pharmacokinetics, Tumor Uptake and Biodistribution by Engineered Nanoparticles. *PLoS One* 2011, **6**, 3–8.
- (35) N. Parameswaran and S. Patial, Tumor necrosis factor-alpha signaling in macrophages.

- Crit. Rev. Eukaryot. Gene Expr. 2010, 20, 87–103.
- (36) J. Son, G. Lee and S. Cha, Direct Analysis of Triacylglycerols from Crude Lipid Mixtures by Gold Nanoparticle-Assisted Laser Desorption/Ionization Mass Spectrometry. *J. Am. Soc. Mass Spectrom.* 2014, **25** (5), 891–894.
- (37) S. N. Jackson, M. Ugarov, T. Egan, J. D. Post, D. Langlais, J. A. Schultz and A. S. Woods, MALDI-Ion Mobility-TOFMS Imaging of Lipids in Rat Brain Tissue. J. Mass Spectrom. 2007, **42**, 1093–1098.
- (38) O. Klein, K. Strohschein, G. Nebrich, M. Fuchs, H. Thiele, P. Giavalisco, G. N. Duda, T. Winkler, J. H. Kobarg, D. Trede and S. Geissler, S. Unraveling Local Tissue Changes within Severely Injured Skeletal Muscles in Response to MSC-Based Intervention Using MALDI Imaging Mass Spectrometry. *Sci. Rep.* 2018, **8**, 12677.
- (39) T. Gemoll, E. Miroll, O. Klein, A. Lischka, M. Eravci, C. Thorns and J. K. Habermann, Spatial UBE2N Protein Expression Indicates Genomic Instability in Colorectal Cancers. *BMC Cancer* 2019, **19**, 710.
- (40) M. Kihara, Y. Matsuo-Tezuka, M. Noguchi-Sasaki, K. Yorozu, M. Kurasawa, Y. Shimonaka and M. Hirata, Visualization of 57 Fe-Labeled Heme Isotopic Fine Structure and Localization of Regions of Erythroblast Maturation in Mouse Spleen by MALDI FTICR-MS Imaging. *J. Am. Soc. Mass Spec.* 2017, **28**, 2469-2475.
- (41) M. Ifuku, T. Katafuchi, S. Mawatari, M. Noda, K. Miake, M. Sugiyama and T. Fujino, Anti-Inflammatory/Anti-Amyloidogenic Effects of Plasmalogens in Lipopolysaccharide-Induced Neuroinflammation in Adult Mice. *J. Neuroinflammation* 2012, **9**, 673.
- (42) A. Irie, K. Yamamoto, Y. Miki and M. Murakami, Phosphatidylethanolamine Dynamics Are Required for Osteoclast Fusion. *Sci. Rep.* 2017, 7, 46715.
- (43) M. F. Cesta, Normal Structure, Function, and Histology of the Spleen. *Toxicol. Pathol.* 2006, **34**, 455-465.
- (44) N. H. Patterson, M. Tuck, R. Van De Plas and R. M. Caprioli, Advanced Registration and Analysis of MALDI Imaging Mass Spectrometry Measurements through Autofluorescence Microscopy. *Anal. Chem.* 2018, **90**, 12395-12403.
- (45) M. A. Jones, S. H. Cho, N. H. Patterson, R. Van de Plas, J. M. Spraggins, M. R. Boothby and R. M. Caprioli, Discovering New Lipidomic Features Using Cell Type Specific Fluorophore Expression to Provide Spatial and Biological Specificity in a Multimodal Workflow with MALDI Imaging Mass Spectrometry. *Anal. Chem.* 2020, **92**, 7079-7086.
- (46) B. Flinders, L. R. S. Huizing, M. van Heerden, F. Cuyckens, U. P. Neumann, L. J. W. van der Laan, S. W. M. Olde Damink, R. M. A. Heeren, F. G. Schaap and R. J. Vreeken, Cross-Species Molecular Imaging of Bile Salts and Lipids in Liver: Identification of Molecular Structural Markers in Health and Disease. *Anal. Chem.* 2018, **90**, 11835-11846.
- (47) R. Weiskirchen, S. K. Meurer, C. Liedtke and M. Huber, Mast Cells in Liver Fibrogenesis. *Cells* 2019, **8**, 1429.

- (48) J. R. Gordon and S. J. Galli, Mast Cells as a Source of Both Preformed and Immunologically Inducible TNF-α/Cachectin. *Nature* 1990, **346**, 274-276.
- (49) R. Singh and J. W. Lillard, Nanoparticle-Based Targeted Drug Delivery. *Exp. Mol. Pathol.* 2009, **86**, 215–223.
- (50) W. Khovidhunkit, M. S. Kim, R. A. Memon, J. K. Shigenaga, A. H. Moser, K. R. Feingold and C. Grunfeld, Effects of Infection and Inflammation on Lipid and Lipoprotein Metabolism: Mechanisms and Consequences to the Host. *J. Lipid Res.* 2004, 45, 1169-1196.
- (51) M. Brust, M. Walker, D. Bethell, D. J. Schiffrin and R. Whyman, Synthesis of Thiol-Derivatised Gold Nanoparticles in a Two-Phase Liquid–Liquid System. *J. Chem. Soc., Chem. Commun.* 1994, 7, 801–802.
- (52) M. J. Hostetler, A. C. Templeton and R. W. Murray, Dynamics of Place-Exchange Reactions on Monolayer-Protected Gold Cluster Molecules. *Langmuir* 1999, **15**, 3782–3789.